

# Estimating Phenotypic Traits From UAV Based RGB Imagery

Javier Ribera  
Video and Image Processing  
Laboratory (VIPER)  
Purdue University  
West Lafayette, Indiana USA

Fangning He  
Digital Photogrammetry  
Research Group (DPRG)  
Purdue University  
West Lafayette, Indiana USA

Yuhao Chen  
Video and Image Processing  
Laboratory (VIPER)  
Purdue University  
West Lafayette, Indiana USA

Ayman F. Habib  
Digital Photogrammetry  
Research Group (DPRG)  
Purdue University  
West Lafayette, Indiana USA

Edward J. Delp  
Video and Image Processing  
Laboratory (VIPER)  
Purdue University  
West Lafayette, Indiana USA

## ABSTRACT

In many agricultural applications one wants to characterize physical properties of plants and use the measurements to predict, for example biomass and environmental influence. This process is known as phenotyping. Traditional collection of phenotypic information is labor-intensive and time-consuming. Use of imagery is becoming popular for phenotyping. In this paper, we present methods to estimate traits of sorghum plants from RGB cameras on board of an unmanned aerial vehicle (UAV). The position and orientation of the imagery together with the coordinates of sparse points along the area of interest are derived through a new triangulation method. A rectified orthophoto mosaic is then generated from the imagery. The number of leaves is estimated and a model-based method to analyze the leaf morphology for leaf segmentation is proposed. We present a statistical model to find the location of each individual sorghum plant.

## Keywords

image segmentation, image-based phenotyping, image rectification

## 1. INTRODUCTION

In many agricultural applications one wants to characterize physical properties of plants and use the measurements to predict, for example, biomass and environmental influence. This process is known as phenotyping. Obtaining high quality phenotypic information is of crucial importance for plant breeders in order to study a crop's performance [1]. Some phenotypic traits such as leaf area have been shown to be correlated with above-ground biomass [2, 3, 4]. Collecting Permission to make digital or hard copies of all or part of this work for personal or classroom use is granted without fee provided that copies are not made or distributed for profit or commercial advantage and that copies bear this notice and the full citation on the first page. Copyrights for components of this work owned by others than the author(s) must be honored. Abstracting with credit is permitted. To copy otherwise, or republish, to post on servers or to redistribute to lists, requires prior specific permission and/or a fee. Request permissions from [permissions@acm.org](mailto:permissions@acm.org).

22nd ACM SIGKDD Conference on Knowledge Discovery and Data Mining 2016 San Francisco, California USA

© 2016 Copyright held by the owner/author(s). Publication rights licensed to ACM. ISBN 978-1-4503-2138-9.

DOI: 10.1145/1235

phenotypic data is often done manually and in a destructive manner.

Computer-assisted methods and in particular image based methods are becoming popular[5, 6]. There are commercial image based systems for automated plant phenotyping [7, 8, 9] that are mainly used indoors. In fact, most image-based phenotyping methods that have been proposed are for indoor or greenhouse settings, while real-life crops are mainly grown outdoors [10]. Many different sensor types have been proposed for phenotyping including multi-spectral, hyper-spectral, IR and RGB images. In this paper we focus on methods that use visible RGB images acquired by a low cost Unmanned Aerial Vehicle (UAV) flying over a field. Our target crop is Sorghum.

In [11], a camera-based growth chamber is described for plant phenotyping using micropots. The plant leaves are segmented by selecting a green cluster in the YIQ colorspace [12]. Leaf morphology is determined using morphological processing and connected components. The number of leaves per plant and the length of each leaf are estimated. In [9] the plant *Setaria* is phenotyped in a highly controlled setting. The phenotypic traits are estimated from RGB images include plant height, convex hull, and plant area using morphological and watershed methods. In [13], the circular geometry and overlap between the leaves of rosette plants are used in order to individually segment each leaf. In [14], rosette plants in a laboratory are automatically segmented and analyzed using active contours and a Gaussian Mixture Model. Other image based methods are described in several review papers and web sites [15, 5, 16].

Low-cost UAVs have recently emerged as a promising geospatial data acquisition system for a wide range of applications including phenotyping [17, 18, 19]. Recent advances in both automated UAV flying and large-field-of-view (LFOV) cameras have increased the utilization of UAVs equipped with low-cost LFOV RGB cameras [20]. Due to the inherent spatial distortion caused by LFOV cameras the images must be corrected before phenotypic measurements can be done. Commercial software can automate the process of 3D image 3D correction and reconstruction. However, utilization of such software for phenotyping remains a challenging task due to the fact that agriculture fields usually contain poor and repetitive texture. This can severely impact the relative

orientation recovery for UAV images.

This paper presents methods that use digital images that are acquired from a low-cost UAV using a large field of view RGB camera (e.g., GoPro Hero 3+ Black Edition). We describe the calibration of the camera to determine its internal characteristics. The position and orientation of the acquired imagery together with the coordinates of sparse points along the area of interest are derived through a proposed triangulation technique. A rectified orthophoto mosaic is then generated by fusing the derived information from the calibration and triangulation information. Finally, the distortion-free images and orthophoto mosaic are used to derive phenotypic traits such as leaf area and count and plant locations.

## 2. ORTOPHOTO GENERATION

As indicated above, the images from our UAV need to be spatially corrected due to the camera's large field of view. The three steps are described below for our proposed correction methods. First, due to severe image distortions caused by the wide-angle lens, camera calibration is done to estimate the internal characteristics of the LFOV camera. Then, Structure from Motion (SfM) [21] is used to take advantage of prior information of the UAV flight trajectory and for automated image orientation recovery and image sparse point cloud generation. Finally, an RGB orthophoto mosaic image of the entire sorghum field is generated. In order to generate this mosaic, the image exterior orientation parameters (EOPs) are estimated, the camera calibration parameters, and the generated point cloud are used.

### 2.1 Camera Calibration

The basis of the camera calibration is bundle adjustment [22] that includes additional parameters that describe the camera's internal characteristics. We demonstrated the capability of using the USGS Simultaneous Multi-frame Analytical Calibration (SMAC) distortion model for both target-based and feature-based calibration of LFOV cameras [23]. The SMAC model is used here for the calibration of the UAV camera. For the SMAC model, all pixel locations  $(x, y)$  must be referenced to the image coordinate system and then translated to the principal point  $(x_p, y_p)$ .  $(\bar{x}, \bar{y})$  are the pixel coordinates after correcting to the principal point using Equation 1.

$$\begin{aligned}\bar{x} &= x - x_p \\ \bar{y} &= y - y_p\end{aligned}\quad (1)$$

For the distortion parameters, both radial and decentering lens distortions are considered. Radial lens distortion is caused by the large off-axial angle and lens manufacturing flaws and are located along a radial direction from the principal point. Radial lens distortion is more significant in LFOV cameras. According to the SMAC model, the correction for the radial lens distortion ( $\Delta x_{RLD}$ ,  $\Delta y_{RLD}$ ) can be expressed as in Equation 2 using the coefficients  $(K_0, K_1, K_2, K_3)$ .

$$\begin{aligned}\Delta x_{RLD} &= \bar{x} [K_0 + K_1(r^2 - R_0^2) + K_2(r^4 - R_0^4) + K_3(r^6 - R_0^6)] \\ \Delta y_{RLD} &= \bar{y} [K_0 + K_1(r^2 - R_0^2) + K_2(r^4 - R_0^4) + K_3(r^6 - R_0^6)]\end{aligned}\quad (2)$$

where  $r = \sqrt{x^2 + y^2}$ ,  $K_0, K_1, K_2$ , and  $K_3$  are the radial lens distortion parameters,  $R_0$  is a camera-specific constant. In

this paper,  $R_0$  is defined as 0 mm. Decentering lens distortion is caused by misalignment of the elements of the lens system along the camera's optical axis. The decentering lens distortion has radial and tangential components. To evaluate the decentering lens distortion ( $\Delta x_{DL D}$ ,  $\Delta y_{DL D}$ ) for the measured points, one can use the coefficients  $(P_1, P_2)$  as shown in Equation 3.

$$\begin{aligned}\Delta x_{DL D} &= P_1(r^2 + 2\bar{x}^2) + 2P_2\bar{x}\bar{y} \\ \Delta y_{DL D} &= 2P_1\bar{x}\bar{y} + P_2(r^2 + 2\bar{y}^2)\end{aligned}\quad (3)$$

where  $P_1$  and  $P_2$  are the decentering lens distortion parameters.

### 2.2 Structure From Motion

The SfM [21] automates the image EOPs recovery as well as the generation of the sparse image-based point cloud. The SfM approach we used was described by He and Habib in [24]. It is based on a 3-step strategy. In the first step, the relative orientation parameters (ROPs) of all possible image stereo pairs are estimated. The estimation of ROPs requires the identification of conjugate points in the set of available images. Therefore, we use the Scale-Invariant Feature Transform (SIFT)[25] on the stereo-images. Using the Euclidean distances between the SIFT descriptors, potential matches are identified [25]. Then, an approach which uses prior information of the UAV flight trajectory is used for the estimation of the ROPs. We assume that the UAV is moving at constant altitude while operating a nadir-looking camera. This is consistent with our UAV operations using onboard gimbals. Therefore a minimum of two point correspondences are required for the estimation of the ROPs. Random Sample Consensus (RANSAC) [26] is used to remove potential outliers among the initial matches. RANSAC is used to find the point-to-epipolar distance of each conjugate point pair using parameters that are derived from different randomly selected point samples. Then an estimate of the ROPs using an iterative procedure is done. This approach is different from the conventional non-linear least-square adjustment in that it is based on a direct linearization of the co-planarity model [27]. The matching outliers are then removed using a normalization process that imposes constraints on the xy-parallax according to epipolar geometry.

Once the ROPs of all possible stereo-pairs are estimated, the image EOPs are initialized. This initialization starts with defining a local coordinate frame using an image triplet that satisfies both a large number of corresponding points and a compatibility configuration [28]. The remaining images are then sequentially augmented into the final image block or trajectory. In order to reduce the effects of error propagation, at each step of the image augmentation, only the image that exhibits the highest compatibility with the previously referenced imagery is selected. Finally, this image is aligned relative to the pre-defined local coordinate system.

The EOPs from the initial recovery are only relative to an arbitrarily defined local reference frame. We transform the estimated EOPs to an absolute orientation and the sparse point cloud to a mapping reference frame. An example is shown in Figure 1. The coordinates of Ground Control Points (GCPs) are derived through a prior GPS survey of the sorghum field. These GCPs are used to establish the absolute orientation. After the estimation of the absolute orien-

tation parameters, a global bundle adjustment is done. This bundle adjustment includes SIFT-based tie points, manually measured image coordinates of the GCPs, and the corresponding GPS-coordinates of these GCPs. This yields the image EOPs and the sparse point-cloud coordinates relative to the GCPs' reference frames. Figure 2 illustrates the inputs and outputs of the global bundle adjustment process.



Figure 1: Reconstructed sparse point cloud, positions and orientations.

### 2.3 RGB Orthophoto Mosaic

Finally, in order to generate the RGB orthophoto, a Digital Elevation Model (DEM) is interpolated from the sparse point cloud, which has been transformed relative to the mapping frame. Then, the DEM, the bundle adjustment-based image EOPs, and the camera calibration parameters are used to produce an RGB orthophoto mosaic of the entire field. An example of the orthophoto is shown in Figure 3.

The conceptual basis for generating an RGB orthophoto mosaic is an object-to-image backward and forward projection process using collinearity equations [27]. It is important to note that, although each pixel from the orthophoto can be visible in multiple UAV images, only the closest one in the mapping frame is utilized for the RGB mosaic.

## 3. IMAGE BASED PHENOTYPING

### 3.1 Leaf Counting

In this section, we present a method for leaf counting without individually segmenting each leaf.

First, the uncorrected image or orthomosaic is converted from RGB to HSV color space [29]. From the image in the

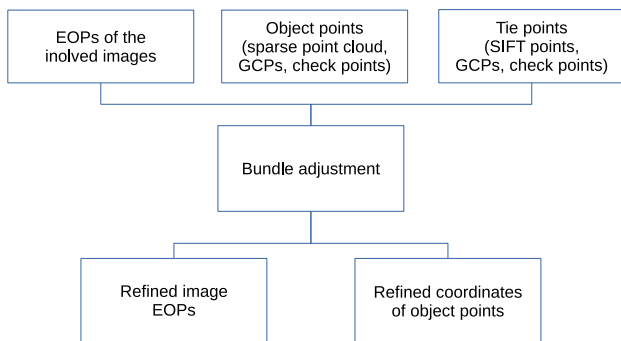


Figure 2: The proposed global bundle adjustment process to transform the image EOPs and sparse point cloud coordinates to the mapping frame.

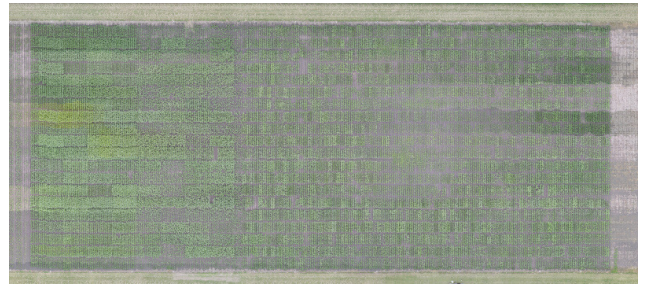


Figure 3: RGB orthophoto of the sorghum field.

HSV color space, a segmentation mask  $Y$  is generated. Each pixel  $Y_m$  in this mask is obtained as:

$$Y_m = \begin{cases} 1 & \text{if } \tau_1 \leq H_m \leq \tau_2 \text{ and } (\tau_3 \leq S_m \text{ or } \tau_4 \leq V_m) \\ 0 & \text{otherwise} \end{cases} \quad (4)$$

where  $H_m$ ,  $S_m$ , and  $V_m$  are the hue, saturation, and value of the pixel  $m$ . The thresholds  $\tau_1, \tau_2, \tau_3$ , and  $\tau_4$  are determined experimentally.  $\tau_1$  and  $\tau_2$  select the characteristic green color of the leaves.  $\tau_3$  and  $\tau_4$  prevent misclassifying some soil pixels as leaves. Then, the number of pixels classified as sorghum leaves is determined as

$$\alpha = \sum_{m=0}^{M-1} Y_m \quad (5)$$

where  $M$  is the number of pixels in the image. This pixel-wise segmentation makes use of the strong color difference between the sorghum leaves, which are generally green or yellow, and the soil and panicles, which are usually brown. An example of the segmentation result is shown in Figure 4.

Now, we want to estimate the number of leaves, denoted as  $\lambda$ , from  $\alpha$ . In order to do this, we assume that number of leaves and the number segmented pixels are linearly related as  $\lambda = \frac{\alpha}{\rho}$ . This assumes that all leaves have approximately the same area. The number of pixels per leaf is  $\rho$ .

In order to calibrate  $\rho$ , a small region of the image is selected. The number of leaves in this region is manually counted and denoted as  $\lambda_0$ . The number of pixels classified as sorghum is denoted as  $\alpha_0$ . Finally,  $\rho$  is estimated by  $\rho = \frac{\alpha_0}{\lambda_0}$ , and the final leaf count can be obtained as  $\lambda = \frac{\alpha}{\rho}$ . We experimentally determined that the relationship between the number of leaves and the number of sorghum pixels is approximately linear at a given growth stage. This

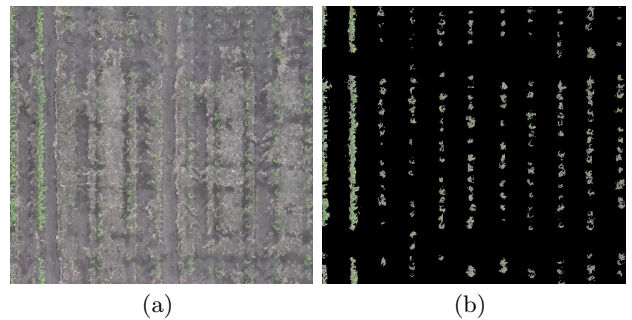
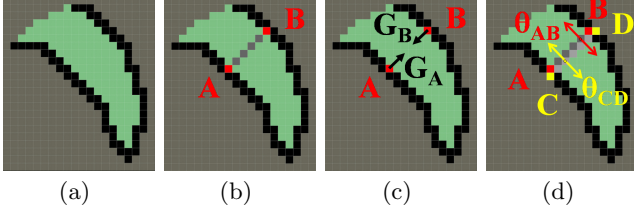


Figure 4: (a) Section of a orthorectified mosaic at an altitude of 15 m. (b) Segmentation result.

method requires that all leaves are at the same distance from the camera. This condition is fulfilled when using the orthorectified mosaic. Also, only leaves that are visible can be counted.

### 3.2 Model Based Leaf Segmentation

Plant leaves have similar morphology but different traits such as leaf length, width and green color hue. From the segmentation of each individual leaf, these traits can be estimated. In this section, we present a shape-based approach to leaf segmentation.



**Figure 5:** (a) A synthetic leaf. (b) A leaf slice connecting two pixels,  $A$  and  $B$ , at opposite edges of the leaf. (c)  $G_A$  and  $G_B$  are the gradient angles of pixels  $A$  and  $B$ . (d)  $\theta_{AB}$  and  $\theta_{CD}$  are the angles the of slices  $S_{AB}$  and  $S_{CD}$ .

$A$  and  $B$  are two pixels located at two opposite edges of a leaf. A pixel-wide line connecting  $A$  and  $B$  is defined as the leaf slice  $S_{AB}$ . Figure 5 depicts these definitions with a synthetic leaf. The gradient angles at  $A$  and  $B$  are  $G_A$  and  $G_B$ , respectively. The angle  $0^\circ$  is defined in the direction of the  $x$  axis.  $G_A$  and  $G_B$  are expected to be opposite to each other with some bias  $T_a$ , i.e.,

$$|G_A - G_B + \pi| \bmod 2\pi < T_a \quad (6)$$

Leaf slices are obtained by using the Stroke Width Transform [30]. The slice angle  $\theta_{AB}$  of  $S_{AB}$  is defined as the normal of the slice (in radians) as

$$\theta_{AB} = \frac{G_A + G_B}{2} \bmod \pi \quad (7)$$

In order to reconstruct leaves from leaf slices, adjacent leaf slices,  $S_{AB}$  and  $S_{CD}$ , are compared. If their angles  $\theta_{AB}$  and  $\theta_{CD}$  differ less than a constant  $T_b$ , i.e.,

$$|\theta_{AB} - \theta_{BC}| < T_b \quad (8)$$

then slices  $S_{AB}$  and  $S_{CD}$  are merged.

Plants with high leaf density can cause leaves overlap with each other. In the case of leaf overlap, there may be a discontinuity between leaf slices as shown in Figure 6.

In this case, the two leaf segments will be merged by the following search method. Let a leaf be split into two leaf segments  $L_1$  and  $L_2$ , separated by a discontinuity, as shown in Figure 6. Let  $S_{AB}$  be the leaf slice with angle  $\theta_{AB}$  at the end of  $L_1$ . Let  $S_{EF}$  be the leaf slice with angle  $\theta_{EF}$  at the end of  $L_2$ . Let  $X_{AB}$  to be a vector contains all the pixels in  $S_{AB}$ . From pixel  $x_i$  in  $X_{AB}$ , we search in the direction of  $\theta_{AB}$ . If a leaf slice  $S_{EF}$  from another leaf  $L_2$  is found and the difference between the two angles is less than a constant  $T_c$ , i.e.,

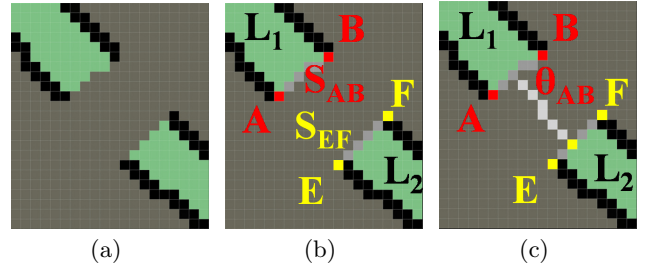


**Figure 6:** (a) A single leaf with a discontinuity that may be due to a leaf crossing. (b) Two leaf segments  $L_1$  and  $L_2$  with almost parallel facing slices  $S_{AB}$  and  $S_{EF}$ . (c) From leaf slice  $S_{AB}$ , we search in the direction of  $\theta_{AB}$  until we find the slice  $S_{EF}$  of the opposite leaf segment  $L_2$ .

$$|\theta_{AB} - \theta_{EF}| < T_c, \quad (9)$$

then leaves segments  $L_1$  and  $L_2$  are considered the same leaf.

Note that the thresholds  $T_a, T_b, T_c$  are determined experimentally. This method addresses leaf discontinuity due to leaf crossing, but requires that leaf edges are clearly distinguishable. Overlap of parallel leaves may lead to undersegmentation.

### 3.3 Plant Location Model

In this section we present a statistical model for segmentation of the plant and determining its location. The location of each plant is defined as the pixel coordinates where the stalk intersects the ground plane and can be used to automatically obtain the inter-row and intra-row spacing. A row of plants is defined as all the plants that are aligned together. Inter-row spacing is defined as the distance between rows. Intra-row spacing is defined as the distance between plants within the same row.

The number of plants in an image is denoted as the constant  $P$  and assumed to be known a priori. The positions of the plants are modeled as a random vector  $X$ , i.e.,

$$X = [X_0, X_1, \dots, X_{P-1}] \quad (10)$$

where  $X_p, p = 0, \dots, P-1$ , contains the  $(i, j)$  coordinates of the  $p$ -th plant:

$$X_p = \begin{bmatrix} X_{p,i} \\ X_{p,j} \end{bmatrix} \quad (11)$$

Our goal is to estimate  $X$  from  $Y$ , where  $Y$  is the color based segmentation mask (Section 3.1).

The 2D coordinates of the pixel  $m$  are denoted as  $K(m)$ . A vector  $Z$  is constructed as

$$Z = [Z_0, Z_1, \dots, Z_{N-1}] \quad (12)$$

where each element  $Z_n = K(n)$ ,  $n = 0, \dots, N-1$ , is included if  $Y_n = 1$ .  $N$  is the number of pixels classified as leaf pixels. Notice that  $N \leq M$ .

The plant  $p$  that is closest to the pixel  $n$  is denoted as  $C(n)$ . The Euclidean distance from the pixel  $n$  to the plant  $C(n)$  is denoted as  $D_n$  and is computed as in Equation 13. Figure 7 depicts the location  $X_p$  of one sorghum plant, and the distance  $D_n$  to a leaf pixel  $n$ .

$$\begin{aligned} D_n &= \|K(n) - K(C(n))\|_2 \\ &= \arg \min_{p=0,1,\dots,P-1} \|K(n) - X_p\|_2 \end{aligned} \quad (13)$$



$$\lim_{\sigma_{p,i} \rightarrow \infty} \hat{X}_p(Z) = \arg \min_{x_p} \left( \frac{1}{\sigma} \sum_{n=1}^N d_n + \frac{1}{2} \left( \frac{x_{p,j} - \mu_{p,j}}{\sigma_{p,j}} \right)^2 \right) \quad (24)$$

Since  $\sigma$  is not known, we estimate it after every Iterative Coordinate Descent (ICD) [31] iteration using the Maximum Likelihood estimator, that can be obtained in closed form:

$$\begin{aligned} \hat{\sigma}(Z, X) &= \arg \max_{\sigma} p_{Z|X, \sigma}(Z|X, \sigma) = \dots \\ &= \frac{1}{N} \sum_{n=0}^{N-1} d_n \end{aligned} \quad (25)$$

#### 4. EXPERIMENTAL RESULTS

The experimental dataset was acquired by a DJI Phantom 2 UAV equipped with a GoPro Hero 3+ Black Edition camera at the Agronomy Center for Research and Education (ACRE) at Purdue University. The UAV was at an altitude of approximately 15 meters and at a speed of roughly 8 m/s. The overlap and side lap percentages for the images are approximately 60%. The ground sampling distance for the images is roughly 1.5cm. The camera is mounted on a gimbal to ensure that images are acquired with the camera's optical axis pointing in the nadir direction, which is consistent with our assumptions for the triangulation approach we described in Section 2.2. To generate the orthophoto mosaic, 18 Ground Control Points (GCPs) and 10 check points are established. Both GCPs and check points were surveyed with a GPS to an approximate accuracy of  $\pm 2$  cm. The root-mean-square error (RMSE) for the check points is evaluated after the bundle adjustment as described in Section 2.3. The outcome from the bundle adjustment is finally used to produce an orthophoto mosaic image. We collected on June 24, 2015 489 images with RMSE for the X, Y, and Z coordinates being 0.04 m, 0.03 m, and 0.05 m, respectively. Figure 3 shows the orthophoto mosaic image. We also collected on July 15, 2015 497 images with RMSE for the X, Y, and Z coordinates being 0.03 m, 0.03 m, and 0.04 m, respectively. Figure 11(a) shows the orthophoto mosaic image. Note that the height and nadir-looking assumptions are only required for stereo-pairs that may be captured along the same flight line or in two different flight lines. Experimental results involving captured datasets by fixed-wing and quad copters have shown that the proposed procedure is quite robust to deviations from such assumptions.

The color-based leaf counting method of Section 3.1 was tested using individual perspective images, the distortion-free images, and the entire orthorectified mosaic. By perspective images we mean the original, non-rectified individual images as they are taken from the camera. The distortion-free images are the perspective images whose lens distortion has been removed. Figure 9 shows the leaf segmentation of a perspective image taken on July 15, 2015. The local density of leaf pixels is also shown as a heat map. The value of a given pixel in the heat map is the number of leaf pixels in the neighborhood of that pixel. The size of the neighborhood was set to  $41 \times 41$  by manually selecting one of the plants. Figure 10 shows the leaf segmentation of a distortion-free image taken on July 15, 2015. Figure 11 shows the leaf segmentation of an orthorectified mosaic. The perspective images used to generate the mosaic were

taken on June 24, 2015. The thresholds we used for these images were experimentally chosen as  $\tau_1 = 30$ ,  $\tau_2 = 79$ ,  $\tau_3 = 30$ , and  $\tau_4 = 163$ . These thresholds are HSV values in the range  $[0, 0, 0]$  to  $[180, 255, 255]$  for 8 bits images. These values may greatly change in different growth stages, and lighting conditions.

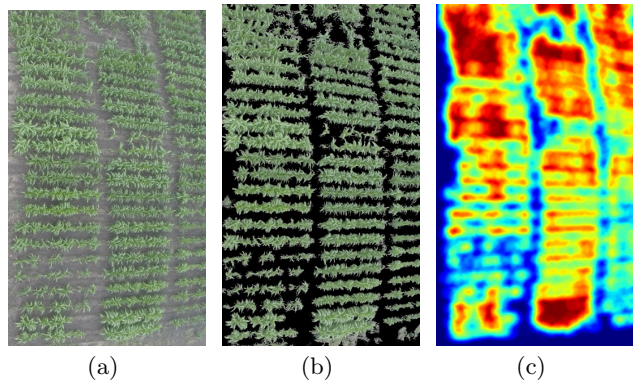


**Figure 9:** (a) Region of a perspective image. (b) Leaf segmentation using the color-based method. (c) Heat map of local leaf density.

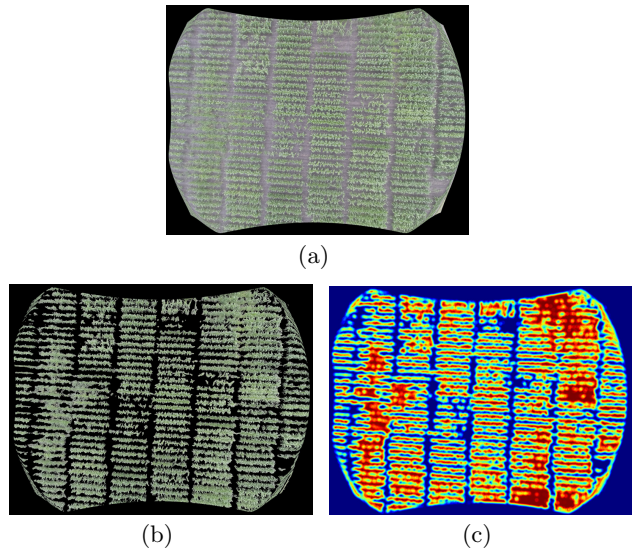


**Figure 10:** (a) Distortion-free image. (b) Leaf segmentation using the color-based method. (c) Heat map of local leaf density.

The leaf segmentation (Section 3.2) was used with the orthophoto shown in Figure 3. A total of 52 Sorghum rows such as the one shown in Figure 12 were analyzed. From the segmentation of each leaf, the leaf count was obtained. The thresholds we used for these images were experimentally chosen as  $T_a = \frac{\pi}{5}$ ,  $T_b = \frac{\pi}{8}$ , and  $T_c = \frac{\pi}{6}$ .

Locations of plants in the orthorectified mosaic of Figure 3 were estimated using the method proposed in Section 3.3. Processing the entire field would take an enormous amount of time. This is because all  $N$  pixel coordinates in  $Z$  are involved into the evaluation of the cost function of Equation 20 for a single candidate  $x_p$  value. In order to reduce

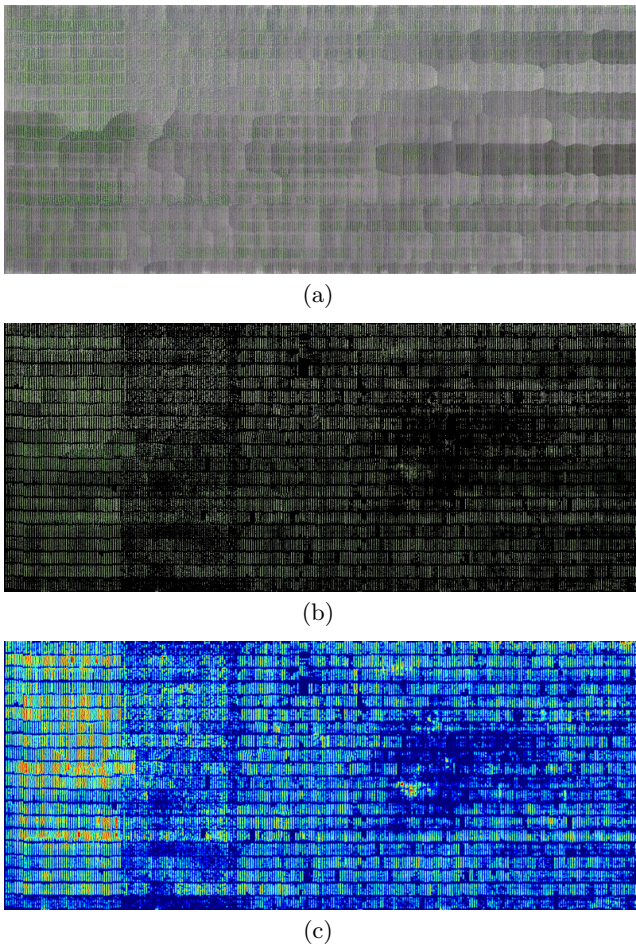


Figure 11: (a) Orthorectified mosaic generated by the procedure explained in Section 2. (b) Segmented leaves. (c) Heat map of local leaf density.

the computational complexity, the mosaic is cropped into regions, and each region is analyzed independently. In Figure 13, the cost function at one iteration is shown. At this iteration, all plant positions are fixed except for one. Note that the coordinate that minimizes the cost function of the free plant is very close to the true position.

## 5. CONCLUSION AND FUTURE WORK

This paper has shown the feasibility of using consumer-grade digital cameras onboard low-cost UAVs for the estimation of plant phenotypic traits. Current and future work will be focusing on the use of the additional sensors such as position and orientation systems as well as LiDAR. Future work will also include image-based plant height determination and the use of leaf angle information for the estimation of the plant center location.

## 6. ACKNOWLEDGMENTS

The information, data, or work presented herein was funded in part by the Advanced Research Projects Agency-Energy (ARPA-E), U.S. Department of Energy, under Award Number DE-AR0000593. The views and opinions of the authors

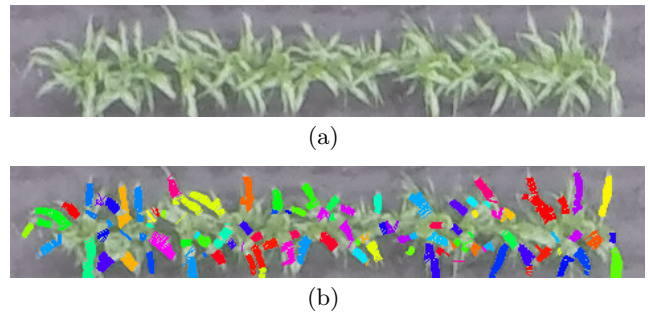


Figure 12: (a) Region of a generated orthomosaic. (b) Leaf segmentation according to Section 3.2.

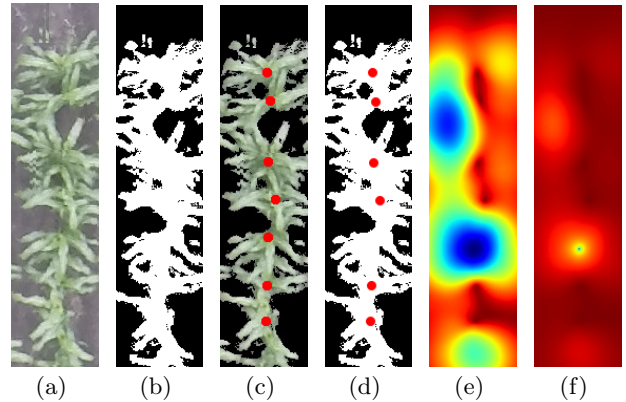


Figure 13: (a) Image showing 7 sorghum plants. (b) Mask  $Y$ , result of the color segmentation of Section 3.1. (c) Red dots are groundtruthed plant locations. (d) Red dots are the fixed plants at this iteration. We are estimating the location of the missing plant. (e) Cost function of Equation 21 (no prior term). The minimum is selected as the location for this plant. Note that the function is non-convex. (f) Cost function in gamma scale to highlight the global minimum.

expressed herein do not necessarily state or reflect those of the United States Government or any agency thereof. Address all correspondence to Edward J. Delp (ace@ecn.purdue.edu).

## 7. REFERENCES

- [1] J. W. White, P. Andrade-Sanchez, M. A. Gore, K. F. Bronson, T. A. Coffelt, M. M. Conley, K. A. Feldmann, A. N. French, J. T. Heun, D. J. Hunsaker, M. A. Jenks, B. A. Kimball, R. L. Roth, R. J. Strand, K. R. Thorp, G. W. Wall, and G. Wang, "Field-based phenomics for plant genetics research," *Field Crops Research*, vol. 133, pp. 101 – 112, July 2012.
- [2] A. A. Gitelson, A. Viña, T. J. Arkebauer, D. C. Rundquist, G. Keydan, and B. Leavitt, "Remote estimation of leaf area index and green leaf biomass in maize canopies," *Geophysical Research Letters*, vol. 30, no. 5, p. 1248, 2003.
- [3] M. R. Golzarian, R. A. Frick, K. Rajendran, B. Berger, S. Roy, M. Tester, and D. S. Lun, "Accurate inference

- of shoot biomass from high-throughput images of cereal plants,” *Plant Methods*, vol. 7, no. 1, pp. 1–11, 2011.
- [4] E. H. Neilson, A. M. Edwards, C. K. Blomstedt, B. Berger, B. L. Møller, and R. M. Gleadow, “Utilization of a high-throughput shoot imaging system to examine the dynamic phenotypic responses of a C<sub>4</sub> cereal crop plant to nitrogen and water deficiency over time,” *Journal of Experimental Botany*, vol. 66, no. 7, pp. 1817–1832, 2015.
- [5] L. Li, Q. Zhang, and D. Huang, “A review of imaging techniques for plant phenotyping,” *Sensors*, vol. 14, no. 11, pp. 20078–20111, 2014.
- [6] S. Sankaran, L. R. Khot, C. Z. Espinoza, S. Jarolmasjed, V. R. Sathuvalli, G. J. Vandemark, P. N. Miklas, A. H. Carter, M. O. Pumphrey, N. R. Knowles, and M. J. Pavék, “Low-altitude, high-resolution aerial imaging systems for row and field crop phenotyping: A review,” *European Journal of Agronomy*, vol. 70, pp. 112–123, October 2015.
- [7] “LemnaTech.” URL: <http://lemnatec.com/>.
- [8] C. Granier, L. Aguirrezabal, K. Chenu, S. J. Cookson, M. Dauzat, P. Hamard, J. Thioux, G. Rolland, S. Bouchier-Combaud, A. Lebaudy, B. Muller, T. Simonneau, and F. Tardieu, “Phenopsis, an automated platform for reproducible phenotyping of plant responses to soil water deficit in *arabidopsis thaliana* permitted the identification of an accession with low sensitivity to soil water deficit,” *New Phytologist*, vol. 169, no. 3, pp. 623–635, 2006.
- [9] N. Fahlgren, M. Feldman, M. A. Gehan, C. S. M. S. Wilson, D. W. Bryant, S. T. Hill, C. J. McEntee, S. N. Warnasooriya, I. Kumar, T. Ficor, S. Turnipseed, K. B. Gilbert, T. P. Brutnell, J. C. Carrington, T. C. Mockler, and I. Baxter, “A versatile phenotyping system and analytics platform reveals diverse temporal responses to water availability in *setaria*,” *Molecular Plant*, June 2015.
- [10] D. Kelly, A. Vatsa, W. Mayham, L. Ngô, A. Thompson, and T. KazicDerek, “An opinion on imaging challenges in phenotyping field crops,” *Machine Vision and Applications*, pp. 1–14, December 2015.
- [11] S. A. Tsiftaris and C. Noutsos, “Plant phenotyping with low cost digital cameras and image analytics,” *Information Technologies in Environmental Engineering*, pp. 238–251, April 2009.
- [12] X. Wu, “Color quantization by dynamic programming and principal analysis,” *ACM Transactions on Graphics*, vol. 11, pp. 348–372, October 1992.
- [13] J. Pape and C. Klukas, “3-d histogram-based segmentation and leaf detection for rosette plants,” *Workshops of the European Conference on Computer Vision*, pp. 61–74, 2014. Zurich, Switzerland.
- [14] M. Minervini, M. M. Abdelsamea, and S. A. Tsiftaris, “Image-based plant phenotyping with incremental learning and active contours,” *Ecological Informatics*, vol. 23, pp. 35–48, 2014.
- [15] N. Fahlgren, M. A. Gehan, and I. Baxter, “Lights, camera, action: high-throughput plant phenotyping is ready for a close-up,” *Current Opinion in Plant Biology*, vol. 24, pp. 93–99, 2015.
- [16] G. Lobet, X. Draye, and C. Périlleux, “An online database for plant image analysis software tools,” *Plant Methods*, vol. 9, no. 38, pp. 1–8, 2013.
- [17] C. V. Tao and J. Li, *Advances in mobile mapping technology*, vol. 4. CRC Press, 2007.
- [18] S. C. Chapman, T. Merz, A. Chan, P. Jackway, S. Hrabar, M. F. Dreccer, E. Holland, B. Zheng, T. J. Ling, and J. Jimenez-Berni, “Pheno-copter: A low-altitude, autonomous remote-sensing robotic helicopter for high-throughput field-based phenotyping,” *Agronomy*, vol. 4, no. 2, pp. 279–301, 2014.
- [19] F. J. Adamsen, J. P. J. Pinter, B. E. M. R. L. LaMorte, G. W. Wall, S. W. Leavitt, and B. A. Kimball, “Measuring wheat senescence with a digital camera,” *Crop Science*, vol. 39, no. 3, pp. 719–724, 1999.
- [20] A. Habib, W. Xiong, F. He, H. L. Yang, and M. Crawford, “Improving orthorectification of uav-based pushbroom scanner imagery using derived orthophotos from frame cameras,” *IEEE Journal of Selected Topics in Applied Earth Observations and Remote Sensing*, p. “To appear”, February 2016.
- [21] M. Westoby, J. Brasington, N. Glasser, M. Hambrey, and J. Reynolds, “Structure-from-Motion photogrammetry: A low-cost, effective tool for geoscience applications,” *Geomorphology*, vol. 179, pp. 300–314, December 2012.
- [22] B. Triggs, P. McLauchlan, and R. Hartley, “Bundle adjustment — a modern synthesis,” *Lecture Notes in Computer Science; Vision Algorithms: Theory and Practice*, pp. 298–372, September 2000. Corfu, Greece.
- [23] F. He and A. Habib, “Target-based and feature-based calibration of low-cost digital cameras with large field-of-view,” *Annual Conference of American Society for Photogrammetry and Remote Sensing (ASPRS)*, May 2015.
- [24] F. He and A. Habib, “Linear approach for initial recovery of the exterior orientation parameters of randomly captured images by low-cost mobile mapping systems,” *The International Archives of Photogrammetry, Remote Sensing and Spatial Information Sciences*, vol. 40, no. 1, p. 149, 2014.
- [25] D. G. Lowe, “Distinctive image features from scale-invariant keypoints,” *International journal of computer vision*, vol. 60, pp. 91–110, November 2004.
- [26] M. A. Fischler and R. C. Bolles, “Random sample consensus: a paradigm for model fitting with applications to image analysis and automated cartography,” *Readings in Computer Vision*, pp. 726–740, 1987.
- [27] E. M. Mikhail, J. S. Bethel, and J. C. McGlone, *Introduction to modern photogrammetry*, vol. 1. John Wiley & Sons Inc, 2001.
- [28] F. He and A. Habib, “Automatic orientation estimation of multiple images with respect to laser data,” *Annual Conference American Society for Photogrammetry and Remote Sensing (ASPRS)*, March 2014. Louisville, KY.
- [29] M. K. Agoston, *Computer Graphics and Geometric Modeling*. Springer London, 2005.
- [30] B. Epshtein, E. Ofek, and Y. Wexler, “Detecting text in natural scenes with stroke width transform,” *Computer Vision and Pattern Recognition (CVPR)*, pp. 2963–2970, June 2010. San Francisco, CA.
- [31] S. J. Wright, “Coordinate descent algorithms,” vol. 151, pp. 3–34, 2015.